

# Supplementary Information: Compromise-Free Scaling of Qubit Speed and Coherence

Miguel J. Carballido,<sup>1,\*</sup> Simon Svab,<sup>1</sup> Rafael S. Eggli,<sup>1</sup> Taras Patlatiuk,<sup>1</sup> Pierre Chevalier Kwon,<sup>1</sup>  
Jonas Schuff,<sup>2</sup> Rahel M. Kaiser,<sup>1</sup> Leon C. Camenzind,<sup>1,†</sup> Ang Li,<sup>3,‡</sup> Natalia Ares,<sup>4</sup>  
Erik P.A.M Bakkers,<sup>3</sup> Stefano Bosco,<sup>1,§</sup> J. Carlos Egues,<sup>1,5</sup> Daniel Loss,<sup>1,6</sup> and Dominik M. Zumbühl<sup>1,¶</sup>

<sup>1</sup>*Department of Physics, University of Basel, Klingelbergstrasse 82, CH-4056 Basel, Switzerland*

<sup>2</sup>*Department of Materials, University of Oxford, Oxford OX1 3PH, United Kingdom*

<sup>3</sup>*Department of Applied Physics, TU Eindhoven, Den Dolech 2, 5612 AZ Eindhoven, The Netherlands*

<sup>4</sup>*Department of Engineering Science, University of Oxford, Oxford OX1 3PJ, United Kingdom*

<sup>5</sup>*Instituto de Física de São Carlos, Universidade de São Paulo, 13560-970 São Carlos, São Paulo, Brazil*

<sup>6</sup>*CEMS, RIKEN, Wako, Saitama 351-0198, Japan*

(Dated: June 25, 2025)

## CONTENTS

S1. <i>g</i> -Factor Renormalization due to SOI under iso-Zeeman Driving	2
S2. Non-Monotonicity of the Qubit Parameters	4
S3. Experimental Error on $f_{\text{Rabi}}$	5
S4. Possible Manifestations of <i>g</i> -Tensor Modulation vs Iso-Zeeman Driving on the Measured Zeeman Vector	6
S5. Impact of the Gate Dielectric Quality on Qubit Coherence	9
S6. Estimation of <i>g</i> -Tensor Modulated Contribution to $f_{\text{Rabi}}$	12
S7. Effect of $\beta$ on Computed and Measured Decoherence Rates	13
S8. 2D Voltage Maps of $f_{\text{Rabi}}$ and $T_2^{\text{Hahn}}$	15
S9. Impact of Control-Axis Noise on the Coherence $T_2^{\text{Rabi}}$ of the Driven Qubit	16
References	17

---

\* [miguel.carballido@unibas.ch](mailto:miguel.carballido@unibas.ch)

† Currently at: CEMS, RIKEN, Wako, Saitama 351-0198, Japan

‡ Currently at: Institute of Microstructure and Properties of Advanced materials, Beijing University of Technology, Beijing, 100124, China

§ Currently at: QuTech and Kavli Institute of Nanoscience, Delft University of Technology, Delft, The Netherlands

¶ [dominik.zumbuhl@unibas.ch](mailto:dominik.zumbuhl@unibas.ch)

### S1. $g$ -FACTOR RENORMALIZATION DUE TO SOI UNDER ISO-ZEEMAN DRIVING

Assuming a harmonic confinement potential along the longitudinal axis of the NW, and in the presence of SOI, the measured  $g$ -factor is renormalized by a Gaussian envelope function [1, 2],

$$g = g_{\text{NW}} \exp\left(-\left(\frac{l_{\text{dot}}}{l_{\text{SO}}}\right)^2\right), \quad (1)$$

where  $g_{\text{NW}}$  is the intrinsic  $g$ -factor derived from the microscopic confinement of the NW,  $l_{\text{dot}}$  is the dot size along the direction of lowest confinement and  $l_{\text{SO}}$  is the spin-orbit length defined here as the distance a hole has to traverse along the NW to have its spin flipped due to SOI.

The application of an oscillating electric field to gate RP in the presence of SOI, gives rise to an oscillating effective magnetic field  $B_{\text{eff}}(t)$ , with magnitude [3],

$$B_{\text{eff}}(t) = 2B \frac{l_{\text{dot}}^2}{l_{\text{SO}}} \frac{eE_{\text{MW}}(t)}{\Delta_{\text{orb}}}, \quad (2)$$

where  $e$  is the elementary charge,  $E_{\text{MW}}$  is the a.c. electric field in the dot generated by the microwaves,  $\Delta_{\text{orb}} = \hbar^2 l_{\text{dot}}^{-2} m_{\text{eff}}^{-1}$  is the orbital level splitting with  $m_{\text{eff}}$  the effective hole mass. The effective magnetic field  $\mathbf{B}_{\text{eff}}(t)$ , drives the Rabi oscillations, at the Rabi frequency  $f_{\text{Rabi}} = g \mu_{\text{B}} |\mathbf{B}_{\text{eff}}| / 2\hbar$ , with  $g$  parallel to  $\mathbf{B}$  and  $\hbar$  Planck's constant.

To stay on resonance, the variation of  $g$ , induced by changes of the electrostatic environment, is compensated with a proportional change of  $\mathbf{B}$ , to match the Larmor frequency set by a fixed MW frequency  $hf_{\text{MW}} = g\mu_{\text{B}}|\mathbf{B}|$ . This effectively makes  $f_{\text{Rabi}}$  independent of  $g$ ,

$$f_{\text{Rabi}} = \frac{f_{\text{L}}}{l_{\text{SO}}} \frac{l_{\text{dot}}^2}{\Delta_{\text{orb}}} \frac{e|E_{\text{MW}}(t)|}{\Delta_{\text{orb}}}. \quad (3)$$

Combining Eqs. 1 and 3, yields the relation between  $g$  and  $f_{\text{Rabi}}$ ,

$$g = g_{\text{NW}} \exp\left(-C \cdot f_{\text{Rabi}}^2\right), \quad (4)$$

with the fitting constant  $C = \Delta_{\text{orb}}^3 m_{\text{eff}} f_{\text{MW}}^{-2} \hbar^{-2} e^{-2} |E_{\text{MW}}|^{-2}$ . Fig. S1 shows the estimated orbital spacings  $\Delta_{\text{orb}}$  as a function of  $V_{\text{L}}$  and  $V_{\text{M}}$  to be roughly constant over the operated voltage range. Here  $|E_{\text{MW}}|$  is constant as the frequency and power of the microwave signal were held constant for all experiments.

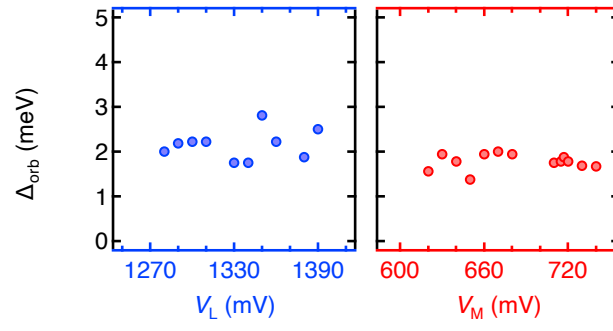


FIG. S1. **Estimation of  $\Delta_{\text{orb}}$ .** Extracted from the ratio between the separation from the bias triangle base line to the first excited state, divided by the triangle height at  $V_{\text{SD}} = 5$  mV, as a function of  $V_L$  (left) and  $V_M$  (right).

## S2. NON-MONOTONICITY OF THE QUBIT PARAMETERS

Because the argument in the exponential suppression of  $g_{\text{NW}}$  solely depends on  $f_{\text{Rabi}} \propto l_{\text{SO}}^{-1}$ , any non-monotonous dependence of the SOI on the gate voltage, represented through  $l_{\text{SO}}(V)$ , is inherited by  $f_{\text{Rabi}}$  and indirectly by the effective  $g$ -factor through the Gaussian term written in Eq. 1 (Main). To provide a more intuitive picture for the latter, in the presence of a magnetic field  $\mathbf{B}$  and from the rest-frame of the quantum dot in the absence of SOI, the envelope function of the dot sees the same spin-polarization along the entire NW, *i.e.*  $g = g_{\text{NW}}$ , as schematically shown in Fig. S2a. When the two lengths  $l_{\text{SO}} \approx l_{\text{dot}}$  become comparable, the envelope function averages over the helical spin texture leading to an effective  $g$ -factor that is suppressed, as schematically shown in Fig. S2b.

The non-monotonic SOI, which both the  $g$ -factor and  $f_{\text{Rabi}}$  depend on, can be explained as follows:

At zero electric field, the structural inversion symmetry of the NW is preserved, leading to a vanishing SOI. When an electric field  $E_x$  is applied perpendicular to a NW with a cylindrical cross-section [4], the inversion symmetry is broken, resulting in an increase of the spin-orbit energy  $E_{\text{SO}} \propto E_x^2$ . As the electric field is further increased, the degree of heavy-hole (HH) and light-hole (LH) mixing gradually changes, until at (much) higher fields, the system begins to resemble a 2D confinement. In this regime, the ground state becomes predominantly HH-like [5], and the linear-in- $k$  direct-Rashba spin-orbit interaction (DRSOI) is weakened due to the large HH-LH splitting  $\Delta_{\text{HH-LH}}$  exceeding 100 meV [6], which governs the strength of the SOI  $\propto \Delta_{\text{HH-LH}}^{-1}$  [7].

In Ge/Si core-shell NWs like the one used in our work, the DRSOI is expected to reach a local maximum at moderate electric fields below 10 MV/m [4, 8, 9]. As mentioned in the main text, these predicted electric field ranges correspond to the voltage range of approximately 100 mV observed around the extrema of  $g$  and  $f_{\text{Rabi}}$  in our Fig. 2a, assuming a voltage drop across a gate pitch of about 50 nm.

While it is difficult to provide a direct “ultimate proof” of the mechanism, our experimental results are consistent with the theoretical framework providing a most plausible explanation for the observed effect, based on the interplay between electric field strength and HH-LH mixing.

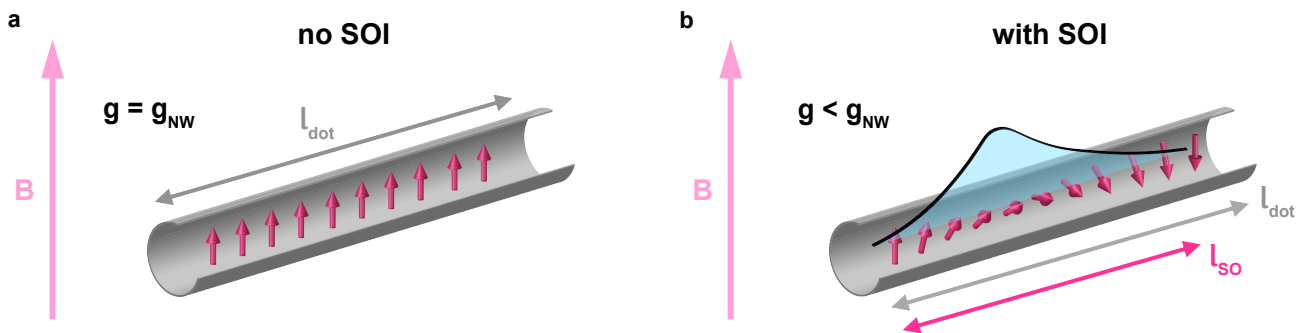


FIG. S2. **Schematic depiction of the spin texture with and without SOI in quasi-1D.** **a**, In the presence of a magnetic field  $\mathbf{B}$  and absence of SOI, the effective  $g$ -factor is constant along the NW. **b**, In the presence of SOI, the envelope function of the dot averages over the helical spin texture leading to a reduced effective  $g$ -factor.

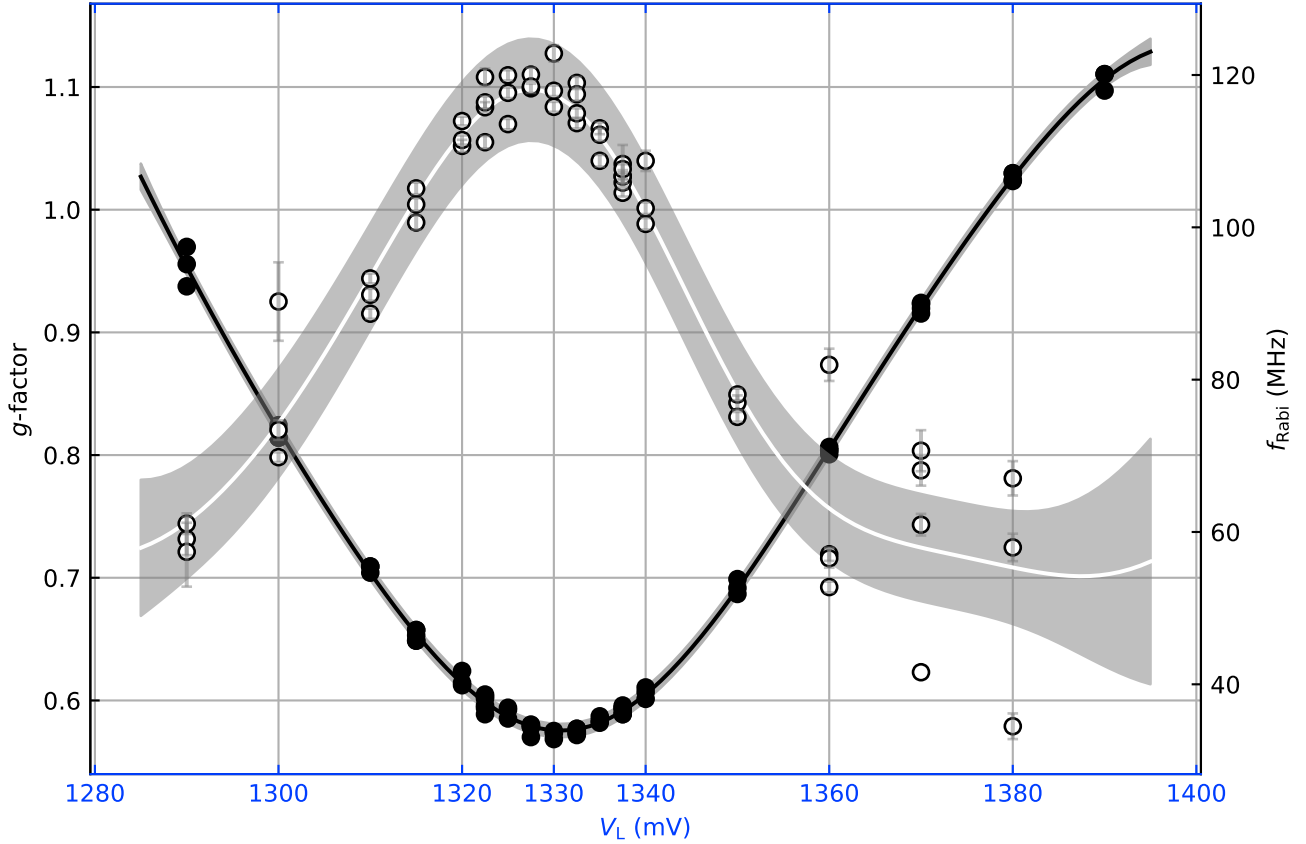
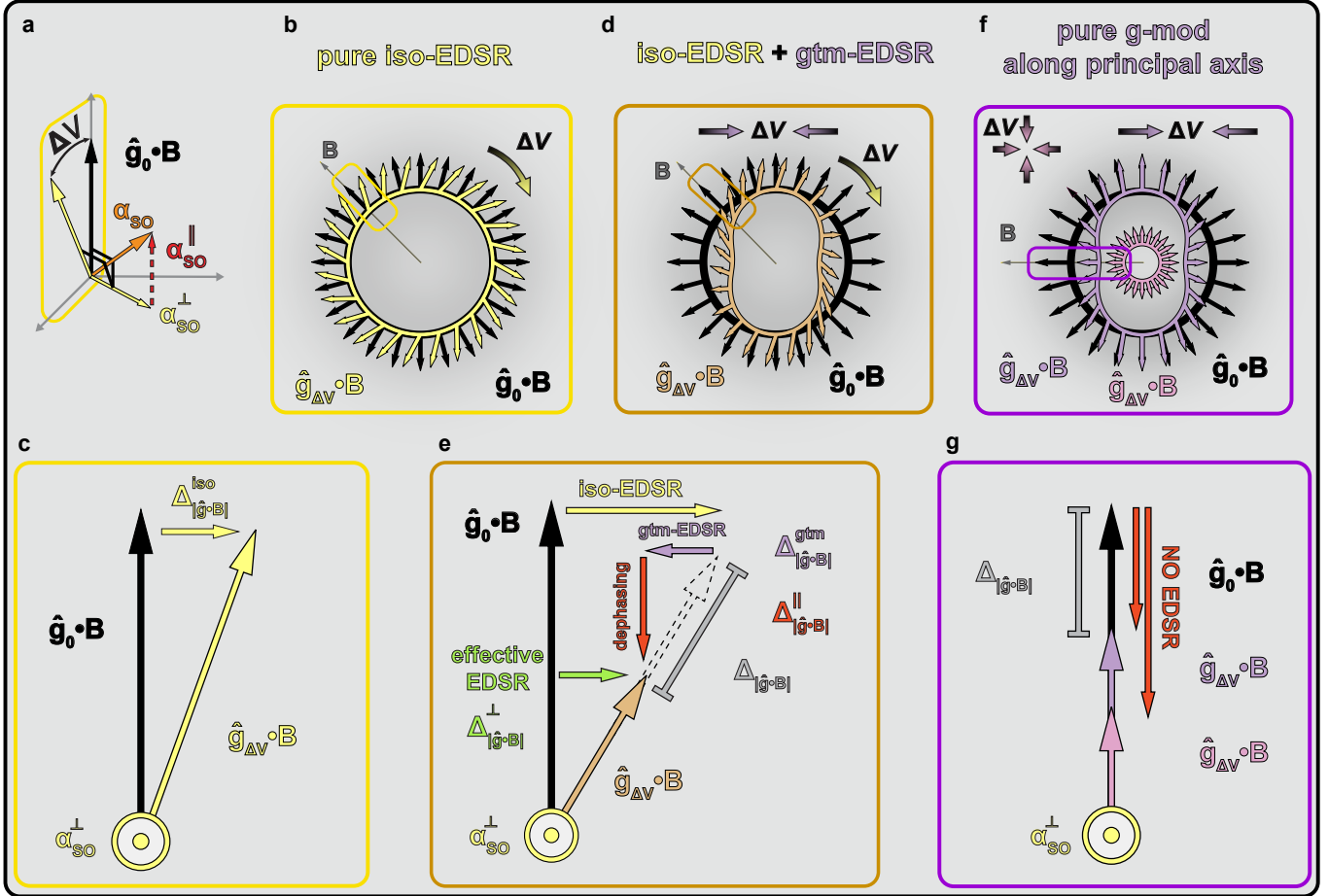
S3. EXPERIMENTAL ERROR ON  $f_{\text{Rabi}}$ 

FIG. S3. **Reproducibility of the extrema in  $f_{\text{Rabi}}$  and  $g$ .** Experimental data of the qubit  $g$ -factor (solid black circles) and Rabi frequency  $f_{\text{Rabi}}$  (open circles), as a function of the left barrier gate voltage  $V_L$ , at fixed gate voltages  $V_M = 660$  mV and  $V_R = 1020$  mV. The fit uncertainty of the measured Rabi oscillations is illustrated by grey error bars. For both the  $g$ -factor and  $f_{\text{Rabi}}$ , Gaussian process fits are applied using a radial basis function kernel. The solid lines denote the average prediction of the Gaussian processes, while the shaded bands show the uncertainty of the Gaussian processes corresponding to one standard deviation.

The data series presented in Fig. S3 was collected in multiple sequences from low to high  $V_L$ . The extremal points of  $f_{\text{Rabi}}$  and  $g$  coincide within 5 mV considering the experimental variation between runs. For  $f_{\text{Rabi}}$  this statistical variation corresponds to  $\sim 10$  MHz around the maximum (approx. 10%), while the variation of the  $g$  is negligibly small.

The observed spread of the measured quantities between runs can be attributed to slight variations of the readout point, in turn slightly varying  $g$  and  $f_{\text{Rabi}}$ . Furthermore, charge switchers which shift the readout point relative to the bias triangle can influence  $g$  and  $f_{\text{Rabi}}$  as well. We note that the traces presented in Fig. S3 were taken at a far later point in time relative to the first measured data points which were presented in the main section. Additionally the sample has experienced several thermal cycles from 1.5 K to 9 K. Taking into account both these circumstances and the reproducibility of the data, speaks for the stability of the device and the observed effects. To more accurately explain differences in the extremal points of  $f_{\text{Rabi}}$  and  $g$  with regards to their positioning in gate voltage  $V_L$ , as well as residual decoherence, a more detailed analytical model must be considered that captures the voltage dependences of the intrinsic NW  $g$ -factor,  $g_{\text{NW}}$  [2, 10], which in this work was assumed to be constant. We would like to direct special attention to Fig. 8b in Ref. [10].

**S4. POSSIBLE MANIFESTATIONS OF G-TENSOR MODULATION VS ISO-ZEEMAN DRIVING ON THE MEASURED ZEEMAN VECTOR**



**FIG. S4. Possible manifestations of qubit driving mechanisms on the measured Zeeman vector.** **a**, Decomposition of the effective spin-orbit vector  $\alpha_{SO}$ , into perpendicular  $\alpha_{SO}^{\perp}$  and parallel  $\alpha_{SO}^{\parallel}$  components relative to  $\hat{g}_0 \cdot \mathbf{B}$ . **b**, Shown in black is the Zeeman vector field of an arbitrary, here isotropic,  $g$ -tensor  $\hat{g}_0$ . Each vector represents a specific direction of magnetic field  $\mathbf{B}$  with constant magnitude. Yellow shows the Zeeman vector field in the case of iso-EDSR, for which the magnitude of an arbitrary Zeeman vector is conserved, and the vector is solely rotated proportional to the strength of SOI and applied amplitude  $\Delta V$ . No distortions of the  $g$ -tensor and therefore Zeeman vector field are present. **c**, Blown up image of one specific direction of  $B$  as indicated in grey in panel b. To first order, the only component acting on the incident Zeeman vector is perpendicular (small angle between  $\hat{g}_0 \cdot \mathbf{B}$  and  $\hat{g}_{\Delta V} \cdot \mathbf{B}$ ). **d**, Zeeman vector field showing the manifestation of both, iso-EDSR and gtm-EDSR (brown). **e**, The length of the Zeeman vector is not conserved. The perpendicular component to the drive originating from modulations of the  $g$ -tensor (violet), in this specific example, counteracts the pure iso-EDSR drive (yellow) resulting in an effective EDSR which induces the Rabi oscillations (green). **f-g**, Edge cases when the  $g$ -tensor modulations occur along the principal magnetic axes (purple) or the dot is symmetrically compressed (or expanded) in the form of a "breathing"-mode (pink), which do not give rise to EDSR.

Provided a constant magnetic field  $\mathbf{B}$ , we capture all effects arising from SOI induced by periodic voltage displacements  $\Delta V$ , by changes of the  $g$ -tensor [11]. Formally, that is  $\hat{g}_0 \cdot \mathbf{B} \xrightarrow{\Delta V} \hat{g}_{\Delta V} \cdot \mathbf{B}$ . Further, we consider solely the vectorial component of the effective spin-orbit vector  $\alpha_{SO}$  that is perpendicular to  $\hat{g}_0 \cdot \mathbf{B}$ , hence  $\alpha_{SO}^{\perp}$ . Mechanisms involving the parallel component of  $\alpha_{SO}$  with respect to  $\hat{g}_0 \cdot \mathbf{B}$ , namely  $\alpha_{SO}^{\parallel}$ , and are responsible for e.g. the longitudinal driving of the spin through the application of an off-resonant microwave tone [12, 13], are not considered here. A vectorial decomposition of  $\alpha_{SO}$  is shown in Fig. S4a.

In the case of SOI mediated Rabi oscillations, we can make a distinction between two EDSR driving mechanisms, based on the way they manifest on the magnitude of the resonant Zeeman vector. When the dot is subject to an infinitesimal change in voltage  $\Delta V$  in the presence of SOI, the action of the induced effective magnetic field  $\mathbf{B}_{SO}$  around which the spin precesses, can

be represented by a rotation of the Zeeman vector  $\hat{\mathbf{g}}_0 \cdot \mathbf{B}$  around  $\alpha_{\text{SO}}^\perp$ .

Assuming no further anisotropies of the  $g$ -tensor are introduced by  $\Delta V$ , we define the induced rotations of the spin that arise while the modulus of the Zeeman vector is conserved, as iso-Zeeman EDSR (iso-EDSR), Fig. S4b. To first order, for a small enough variation  $\Delta V$ , and thus small angle between  $\hat{\mathbf{g}}_0 \cdot \mathbf{B}$  and  $\hat{\mathbf{g}}_{\Delta V} \cdot \mathbf{B}$ , the only component acting on the incident Zeeman vector  $\hat{\mathbf{g}}_0 \cdot \mathbf{B}$  is perpendicular,  $\Delta_{|\hat{\mathbf{g}} \cdot \mathbf{B}|}^{\text{iso}}$ , Figs. S4c. As outlined in [3], iso-EDSR is expected to be the dominant qubit driving mechanism, whenever the motion of the dot induced by periodic voltage shifts  $\Delta V$  does not come along significant variations of the dot potential.

Next, we classify contributions to EDSR that do not conserve the modulus of  $\hat{\mathbf{g}}_0 \cdot \mathbf{B}$  as  $g$ -tensor modulated EDSR (gtm-EDSR). It arises whenever changes in the dot potential modulate the magnetic axes of the  $g$ -tensor and as a result anisotropically modify the Zeeman vector field, Fig. S4d. This mechanism introduces both, perpendicular  $\Delta_{|\hat{\mathbf{g}} \cdot \mathbf{B}|}^{\text{gtm}}$  and parallel  $\Delta_{|\hat{\mathbf{g}} \cdot \mathbf{B}|}^{\parallel}$  components to the incident Zeeman vector, Fig. S4e. Usually, iso-EDSR is accompanied by gtm-EDSR, due to the fact that voltage changes on the gates which displace the dot likely also affect the potential landscape. In such cases, gtm-EDSR can counter act (or enhance) the driving component expected from pure iso-EDSR, yielding an effective EDSR drive  $\Delta_{|\hat{\mathbf{g}} \cdot \mathbf{B}|}^\perp = \Delta_{|\hat{\mathbf{g}} \cdot \mathbf{B}|}^{\text{iso}} \pm \Delta_{|\hat{\mathbf{g}} \cdot \mathbf{B}|}^{\text{gtm}}$ . It is not directly possible to derive the driving strength caused by gtm-EDSR from only measuring  $\Delta_{|\hat{\mathbf{g}} \cdot \mathbf{B}|}$ , as it is the case in our experiments. However, this absolute change in magnitude of the Zeeman vector does provide an upper bound on the  $g$ -tensor modulated contribution to the Rabi oscillations,  $J_{\text{Rabi}}^{\text{gtm}} \propto \Delta_{|\hat{\mathbf{g}} \cdot \mathbf{B}|}^{\text{gtm}}$ .

Finally, there remain some corner cases of highly symmetric modulations of the dot potential ("breathing modes"), or specific orientations of  $\mathbf{B}$  which affect solely the principal magnetic axis longitudinally, and can be considered as pure  $g$ -tensor modulation, Fig. S4f. These scenarios however do not lead to Rabi oscillations, as they lack components perpendicular to the incident Zeeman vector and therefore do not induce EDSR, Fig. S4g.

The simplest Hamiltonian to describe pure iso-EDSR in our system can be obtained following Ref. [14], where an expression is derived to describe the precession of a spin induced by the effective magnetic field that arises due to SOI.

We use the coordinate system introduced in Fig. 1 of the main text. Our Hamiltonian consists of a kinetic term, a harmonic confinement term along the  $y$ -axis (longitudinal axis of the NW) corresponding to the axis of weakest confinement, a Zeeman term with magnetic field  $\mathbf{B} = (B_x, 0, 0)$ , an oscillating electric field along the  $y$ -direction  $\mathbf{E}_{\text{ac}} = E_0 \cos(\omega_{\text{ac}} t)$ , and a spin orbit term with spin-orbit strength  $\alpha_{\text{SO}}^\perp$  which is perpendicular to  $\mathbf{B}$  and the longitudinal axis of the NW, yielding:

$$H_{\text{EDSR}}^{\text{iso}} = \frac{\hbar^2 \hat{k}_y^2}{2m_{\text{eff}}} + \frac{1}{2} m_{\text{eff}} \omega_0^2 y^2 + \frac{1}{2} g_{\text{NW}} \mu_B B_x \hat{\sigma}_x + e E_0 \cos(\omega_{\text{ac}} t) y + \alpha_{\text{SO}}^\perp \hat{\sigma}_z \hat{k}_y \quad ,$$

where  $\hbar$  is the reduced Planck Constant,  $m_{\text{eff}}$  is the effective electron mass,  $\hat{k}_y$  is the 1D momentum operator along the  $y$ -direction,  $\omega_0$  is a constant for the parabolic confinement potential,  $\omega_{\text{ac}}$  is the frequency of the applied ac-field,  $g_{\text{NW}}$  is the intrinsic NW  $g$ -factor,  $\mu_B$  is the Bohr magneton,  $\hat{\sigma}_i$  are the spin-1/2 Pauli operators and  $e$  is the elementary charge.

With the momentum of the dot set along  $\hat{k}_y$ , the SOI Hamiltonian would more generally read  $\alpha_{\text{SO}} \mathbf{n} \cdot \hat{\sigma} \hat{k}_y$ . Here, the parameter representing the spin-orbit strength  $\alpha_{\text{SO}}$  is inversely proportional to the subband splitting between heavy (HH) and light (LH) holes  $\alpha_{\text{SO}} \propto \Delta_{\text{HH-LH}}^{-1} \approx (20 \text{ mV})^{-1}$  and is obtained by a down-projection from the Luttinger-Kohn Hamiltonian onto the lowest energy HH-LH subspace [9, 15].

The normal vector  $\mathbf{n}$  selects the direction of the spin-orbit vector, and depends non-trivially on the static electric field  $\mathbf{E}$  that is used to break the inversion symmetry as well as strain. Relative to the magnetic field  $\mathbf{B}$ , one can define a component of the

spin-orbit vector  $\alpha_{\text{SO}} = \alpha_{\text{SO}} \mathbf{n}$  that is perpendicular,  $\mathbf{B} \perp \alpha_{\text{SO}}^\perp$ , and one that is parallel,  $\mathbf{B} \parallel \alpha_{\text{SO}}^\parallel$ . When driving at resonance,  $\omega_{\text{ac}} = \omega_{\text{L}}$ , the component that induces Rabi oscillations is  $\alpha_{\text{SO}}^\perp$  (where  $|\alpha_{\text{SO}}^\perp| = \alpha_{\text{SO}}^\perp$ ). In the Hamiltonian above, we chose this component to act along the z-direction, perpendicular to both the magnetic field and the longitudinal axis of the NW.

In an ideal setup, we expect the maximal value of  $\alpha_{\text{SO}}$  to enter the Hamiltonian. However, without a vector magnet to precisely calibrate the magnetic field direction, it is unlikely to perfectly reach the conditions of  $\mathbf{B} \perp \alpha_{\text{SO}}$  or  $\mathbf{B} \parallel \alpha_{\text{SO}}$ . Thus, for angles in between, there is likely always a component of  $\alpha_{\text{SO}}$  that will be perpendicular to  $\mathbf{B}$  around which the spin can precess. The component of the spin-orbit vector  $\alpha_{\text{SO}}$  that points parallel to  $\mathbf{B}$ , *i.e.*  $\alpha_{\text{SO}}^\parallel$ , has no effect on the spin unless a far off-resonant microwave tone is applied to induce longitudinal driving of the spin [13].

## S5. IMPACT OF THE GATE DIELECTRIC QUALITY ON QUBIT COHERENCE

Couplings to charge noise originating from impure oxides close to the quantum dot, in which the spin qubit is embedded, pose a limit for coherence [16, 17]. For the Ge/Si NW devices discussed in this work, the closest suspects are the native Silicon oxide on the shell of the nanowire and the ALD-grown  $\text{Al}_2\text{O}_3$  oxide used as gate dielectric. Here, we investigate the impact of ALD-grown gate dielectric quality on the qubit coherence of our devices.

It has been reported that annealing of oxides can remove trapped charges at the oxide-semiconductor interface [18]. We thus compare whether an annealed ALD-grown oxide layer shows any improvement of qubit coherence times as compared to an untreated oxide. To qualitatively assess the dielectric quality, we perform capacitance-voltage (CV) profiling experiments on test-metal-oxide-semiconductor-capacitor devices (MOSCAP), as described in Fig. S5a. The MOSCAPs consist of a material stack resembling that of the qubit devices, but with the difference of using a less resistive heavily p-doped Si substrate to facilitate the capacitance measurements. A DC voltage  $V_G$  from a DAC (Basel Precision Instruments SP927) is combined with an AC voltage  $V_{AC}$  generated by a lock-in amplifier (Stanford Research Systems SR830) and connected to the metal contact of a MOSCAP with a needle prober. The other needle is placed on a region with the exposed p-doped Si substrate and connected to an IV converter (Basel Precision Instruments SP983c), which is then fed back to the lock-in amplifier. The capacitance is calculated from:

$$C = \frac{I_{AC}^Y}{2\pi f V_{AC}} \quad , \quad (5)$$

where  $I_{AC}^Y$  is the measured out-of-phase component of the current signal, and  $f$  the lock-in frequency. Upon measuring the CV-curves of the untreated MOSCAP devices, they are annealed in a rapid thermal annealing oven (MBE-Komponenten GmbH AO500). The CV-curves of the devices annealed at different temperatures are shown in Fig. S5b for increasing duration or temperature. The hysteretic behavior of the curves observed in Fig. S5b can be attributed to undesired interface charge traps between the semiconductor and the oxide [19]. This feature is used as a crude indicator for the oxide quality. Subsequent annealing runs significantly reduce the level of the observed hysteresis and are thus associated with an improvement of the dielectric quality. We note that temperatures beyond  $300^\circ\text{C}$  were not tested to prevent damage to the Ti/Pd bottom gates of the devices. From  $400^\circ\text{C}$  onwards, the bottom gates would show strong signs of deformation.

In summary, we attribute the reduction of hysteresis observed in the CV-curves taken after a  $300^\circ\text{C}$  annealing step, to a qualitative improvement of the interface between the p-type substrate and the  $\text{Al}_2\text{O}_3$  oxide. A more thorough analysis would require to also test the effect of annealing on undoped substrate along with performing measurements at cryogenic temperatures. A further limitation is posed by directly probing the chip surface rather than fabricating an ohmic contact to the doped Si substrate, leading to gate voltage offsets due to the needle-semiconductor contact-interface. To investigate any effects of the annealed ALD oxide on qubit coherence, we compare  $T_2^*$  and  $T_2^{\text{Hahn}}$  measured in the annealed device (described in the main text) with the values in an unannealed device, whose measured data are overlaid in Fig. S5c and S5d. We note that for the given bias triangle in the unannealed qubit device, no dependence of the qubit coherence on the center gate voltage was observed. Further, no clear difference in coherence times can be observed between both devices, indicating that annealing of the ALD oxide layer did not noticeably improve the qubit quality.

We therefore suspect the main source of charge noise to be the native Silicon oxide on the nanowire shell, and our coherence to be dominantly limited by  $T_2$  processes and not  $T_1$  processes (see comment further below). From a materials perspective,

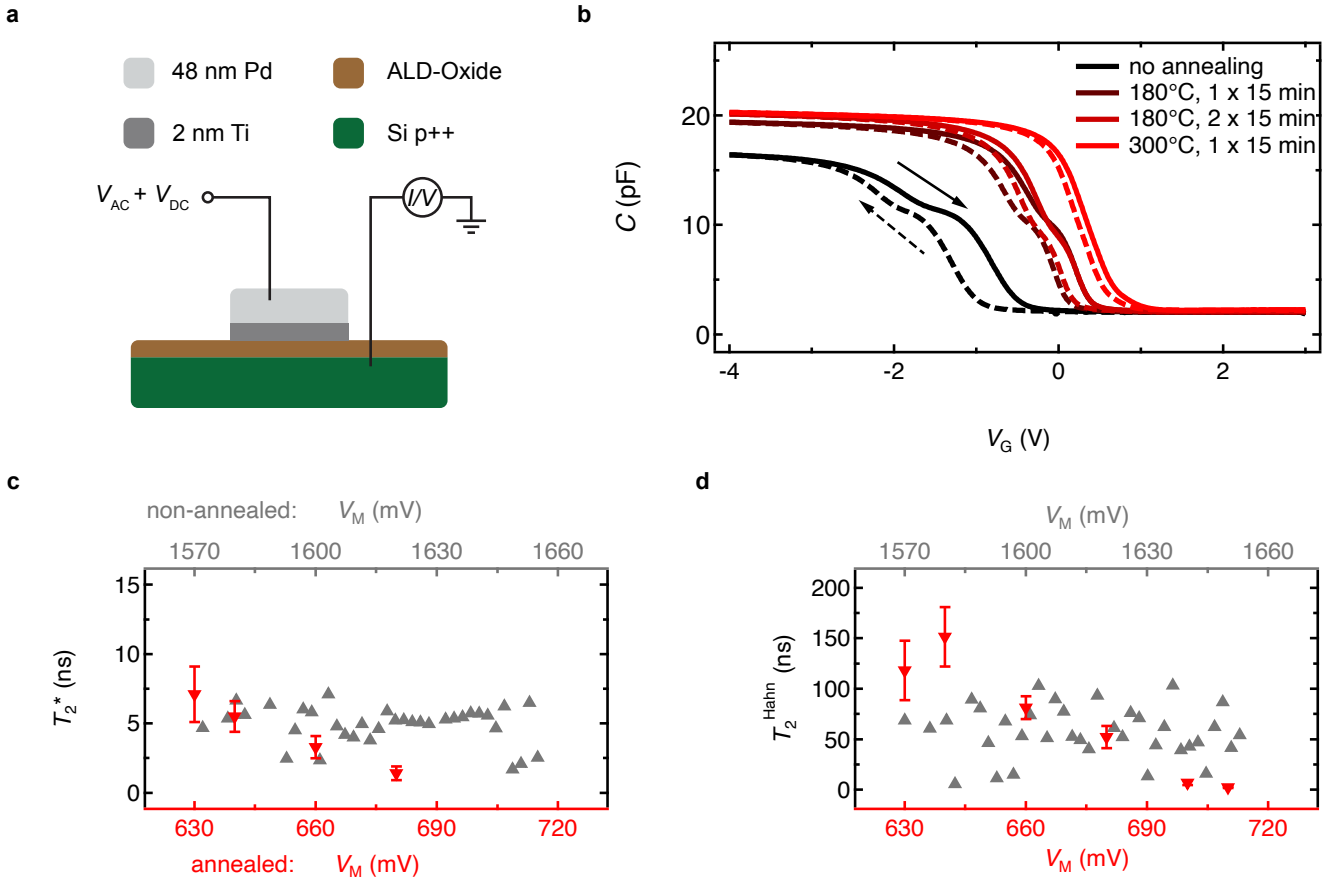


FIG. S5. **Impact of Gate Dielectric Quality on Qubit Coherence.** **a**, Schematic of the MOSCAP used for CV profiling. The device consists of a heavily p-doped Si-substrate covered by  $\sim 24$  nm of ALD-oxide grown on top of the native Si-oxide of the substrate. The top electrode is defined by an  $80 \mu\text{m} \times 80 \mu\text{m}$  Ti/Pd square. **b**, CV-curves of a MOSCAP taken as a reference prior to (black), and after subsequent annealing runs. The temperatures and durations are indicated in the legend. The sweep directions are indicated by the arrows. **c**, Measured values of the Ramsey free evolution time  $T_2^*$  as a function of gate voltage  $V_M$  for the non-annealed device (grey) and the annealed device (red). **d**, Same as c but measuring the free evolution time of a Hahn-Echo experiment  $T_2^{\text{Hahn}}$ . Error bars correspond to standard deviations that result from fitting.

first steps towards improved coherence may focus on improving the quality of interfaces and surfaces [20] by, for example, terminating the Si-shell with high quality thermal oxides within the growth chamber, as opposed to native oxides that grow in an uncontrolled environment when the material is exposed to ambient air.

**Additional Comment on  $T_1$ :** As measured in similar NW devices [21],  $T_1$  is expected to be *ca.* 200 – 500  $\mu\text{s}$  for the magnetic fields we operate our qubits at, which is orders of magnitude longer than the recorded  $T_2$  times.

It is nevertheless important to think about scenarios where the coherence may become  $T_1$ -limited. For example, when the spin qubit were to be strongly coupled to a non-ideal resonator, whereby the losses of the cavity to the photon bath will impact  $T_1$  of the spin qubit (Purcell effect).

In the occasion that the qubit were indeed limited by  $T_1$ -processes, there still is a remedy to counteract this problem by going to higher magnetic fields. The gate speed (here represented by the Rabi frequency  $f_{\text{Rabi}}$ ) scales linearly with the spin-orbit coupling strength  $\alpha_{\text{SO}}$  and linearly with the Larmor frequency  $\omega_L$ , and hence the magnetic field  $B$ , such that  $f_{\text{Rabi}} \propto \omega_L \alpha_{\text{SO}} \propto B \alpha_{\text{SO}}$ . Furthermore, the  $T_1$ -decay rate  $\Gamma_1 = 1/T_1$  (which we wish to be small) scales quadratically with  $\alpha_{\text{SO}}$  but inverse proportionally with  $\omega_L$ , such that  $\Gamma_1 \propto \alpha_{\text{SO}}^2/\omega_L \propto B^2/\omega_L$ . The ratio of the two yields an expression  $f_{\text{Rabi}}/\Gamma_1 \propto \omega_L^2/\alpha_{\text{SO}} \propto B^2/\alpha_{\text{SO}}$ . As can be

seen, the detrimental effect of stronger SOI could be compensated by operating the qubit at slightly higher magnetic fields.

### S6. ESTIMATION OF $g$ -TENSOR MODULATED CONTRIBUTION TO $f_{\text{Rabi}}$

To first order a periodic voltage fluctuation  $dV_{\text{RP}}$  on the driving gate RP, will give rise to a gtm-EDSR contribution of magnitude [22],

$$f_{\text{Rabi}}^{\text{gtm}}(V) = \frac{\eta}{2} \frac{\partial g(V)}{\partial V_{\text{RP}}} \frac{\mu_{\text{B}}}{h} B V_{\text{MW}} \quad , \quad (6)$$

where  $V_{\text{MW}}$  is the amplitude of the microwave voltage applied to gate RP,  $\partial g/\partial V_{\text{RP}}$  is the response of the  $g$ -factor to a variation  $V_{\text{RP}}$ ,  $\mu_{\text{B}}$  Bohr's magneton,  $h$  Planck's constant,  $B$  is the magnetic field amplitude at the qubit resonance and  $\eta$  is an efficiency accounting for the distance from the driving gate to the assumed qubit location over gate LP. The applied microwave voltage arriving at the sample is  $V_{\text{MW}} = 7.8$  mV and was obtained from a power calibration. To estimate the efficiency  $\eta$ , we estimate the horizontal and vertical distance of the expected qubit location relative to the driving gate,  $d_{\text{hor}} = 100$  nm and  $d_{\text{vert}} = 30$  nm (accounting for  $\sim 20$  nm of dielectric and the NW radius of 10 nm). This roughly results in  $\eta \approx 30\%$ .

As explained in Sec. S4  $\partial g/\partial V_i$  provides solely an upper bound to the perpendicular component relevant for the  $g$ -modulated drive. Based on this estimate, datapoints with contributions to the measured Rabi frequencies above  $f_{\text{Rabi}}^{\text{gtm}}/f_{\text{Rabi}} \geq 15\%$  of the measured value of  $f_{\text{Rabi}}$  are considered significantly affected by  $g$ -tensor modulation and were excluded from the fit in Fig. 2g of the main text. The calculated percentages of  $f_{\text{Rabi}}^{\text{gtm}}/f_{\text{Rabi}}$  are shown in Fig. S6.

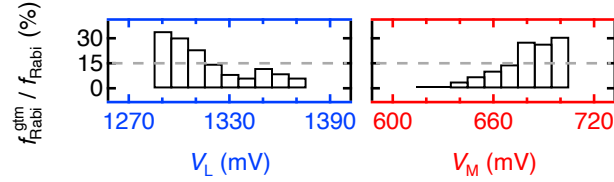


FIG. S6. **Ratio of  $f_{\text{Rabi}}^{\text{gtm}}/f_{\text{Rabi}}$ .** Calculated contribution to  $f_{\text{Rabi}}$  coming from gtm-EDSR represented as the bars. The dashed line corresponds to 15% which was used as our threshold for classification.

## S7. EFFECT OF $\beta$ ON COMPUTED AND MEASURED DECOHERENCE RATES

The best fit of the Hahn-decays was obtained for  $\beta = 0$ . We further note that the qualitative feature of the coherence sweet spot is robust with respect to the choice of  $\beta$  as seen in Figs. S7a-d. We provide an exemplary Hahn-echo data set in Fig. S8 below. The point at  $V_L = 1330$  mV shows some stronger dependence on the choice of noise exponent as opposed to the other points which we explain in the following. Overall, the nature of transport measurements performed in this work, sets an upper bound to the free evolution time  $\tau$  of the Hahn measurements. If each hole loaded into the double dot were to be measured with efficiency  $\eta = 1$ , we would expect the maximum possible current  $e/t_{\text{cycle}}$ , where  $e$  is the elementary charge and  $t_{\text{cycle}} = 2 \times (t_\pi + 2t_{\pi/2} + 2\tau)$ , which yields  $e/t_{\text{cycle}} \approx 1$  pA for  $t_{\text{cycle}} \approx 150$  ns. The leakage currents of our experiments however correspond to efficiencies on the order of  $\eta_{\text{meas}} \approx 0.1$ . This inefficiency can be attributed to co-tunneling events, the inefficient loading of the double dot due to the elevated temperature of operation of 1.5 K or random variations of the device behaviour after a thermal cycle of the device. In the case of  $V_L = 1330$  mV, the highest  $\tau$  used did not suffice to observe a significant characteristic decay of the Hahn-echo. Further increasing of  $\tau$  would have lead to transport currents which are too small to measure. Therefore in this case, the fit was more sensitive on the choice of  $\beta$ .

For the models of decoherence rates for non-zero  $\beta$ , we use the generic expression as derived in the Supplementary Information of [23]:

$$\frac{1}{T_2^{\text{Hahn}}} = 2\pi \left( C_\beta f_0^\beta \sum_i \left( \frac{\partial g}{\partial V_i} S_G \right)^2 \right)^{\frac{1}{\beta+1}}, \quad (7)$$

with  $C_\beta = 2 \sin(\frac{\beta\pi}{2})(2^{1-\beta} - 1)\Gamma(-1-\beta)$ ,  $\Gamma$ , the Gamma function  $\Gamma$ , and  $S_G = S_G(f_0/f)$  is the noise spectral density at reference frequency  $f_0 \approx 12.5$  MHz for our measurements.

**Details of the Fit Procedure:** To be more precise, one may also write  $T_2^{\text{Hahn}}(V_L)$  and  $\frac{\partial g}{\partial V_i}(V_L)$  to denote that these are both functions of  $V_L$ . We hereby assumed one global value for the noise spectrum  $S_G$  ( $S_{G,i} = S_G$ ) weighting each of the  $\frac{\partial g}{\partial V_i}(V_L)$  equally, as we believe the main source of noise to be the native SiO<sub>2</sub> shell homogeneously covering the NW. The position and hence the susceptibility to the noise background is then again reflected by the range of amplitude of each of the curves  $\frac{\partial g}{\partial V_i}(V_L)$  in panels 3b-f in the main text, and corresponds to the location of the qubit relative to the gates, *i.e.* the farther away the gate, the smaller the range of values of  $\frac{\partial g}{\partial V_i}(V_L)$ . The least squared fit we perform takes into account all values of  $V_L$  and the fit coefficient provided is the one which simultaneously minimized the differences between fitted and the experimentally measured values of  $T_2^{\text{Hahn}}(V_L)$  for their specific values of  $V_L$ . This means that all of the five curves and each of their data points in  $\frac{\partial g}{\partial V_i}(V_L)$  were taken into account with their corresponding values of  $V_L$  to perform the fit and we did not pick a single specific value  $V_L = V_L^*$  at a specific gate-voltage.

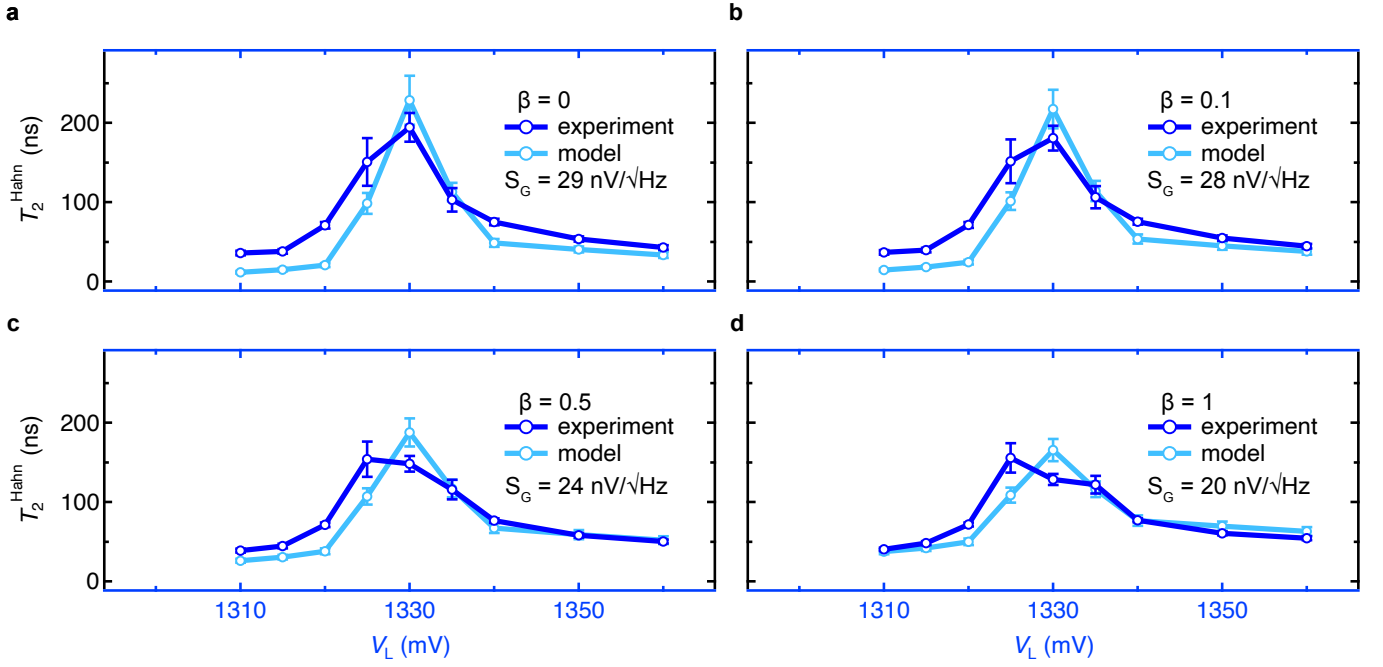


FIG. S7. **Analysis of the experimental Hahn-echo data and model for  $\beta \in \{0, 0.1, 0.5, 1\}$ .** **a**, Identical traces as presented in Fig. 3a of the main text for  $\beta = 0$ . **b-d**, Traces for  $\beta \in \{0.1, 0.5, 1\}$ . All models for non-zero  $\beta$  were computed using Eq. 7. Error bars correspond to standard deviations that result from fitting.

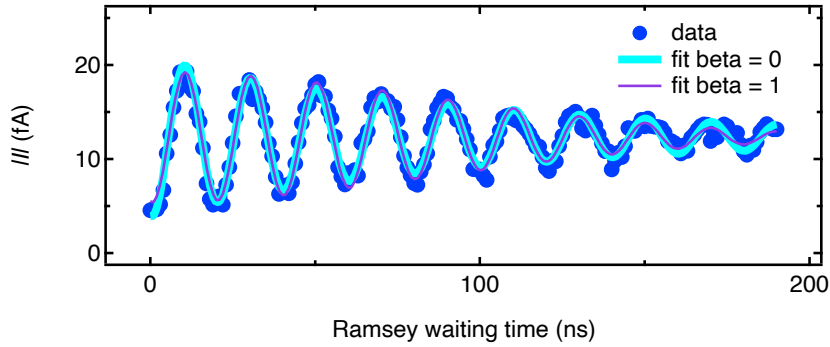


FIG. S8. **Exemplary data set of a Hahn-echo experiment at  $V_L = 1335$  mV.** The qubit state is initialised along the quantization axis ( $z$ -axis). The pulse sequence applied to the qubit consists of a  $\pi_x/2$ -pulse to bring the initial state into the equatorial plane. This is followed by a waiting time  $\tau$  after which a  $\pi_x$ -pulse is applied to refocus the state during a waiting time of  $\tau$ . Finally a second  $\pi_x/2$ -pulse is applied in order to measure the qubit state along the quantization axis. The data points in blue show the current amplitude as a function of waiting time  $\tau$  between the  $\pi/2$ -pulse and the  $\pi$ -refocussing pulse. In keeping with the Supplementary Information S6 we show the data points of the Hahn-echo experiment with both  $\beta = 0$  and  $\beta = 1$ , yielding  $T_{2,\beta=0}^{\text{Hahn}} = 103 \pm 15$  ns and  $T_{2,\beta=1}^{\text{Hahn}} = 122 \pm 11$  ns, respectively. The frequency at which the phase of the second pulse  $\pi_x/2$  varied was set to  $f_\varphi = 50$  MHz. The errors correspond to standard deviations that result from fitting.

### S8. 2D VOLTAGE MAPS OF $f_{\text{Rabi}}$ AND $T_2^{\text{Hahn}}$

To emphasize the overlap of maxima of  $T_2^{\text{Hahn}}$  and  $f_{\text{Rabi}}$ , we present in Fig. S9a the 2D-voltage dependence of  $T_2^{\text{Hahn}}$ , which was already introduced in the main text, as well as the 2D-voltage dependence of  $f_{\text{Rabi}}$  in Fig. S9b, of which only the contours were presented in the main text. Finally, Fig. S9c is obtained by overlaying the contours of the interpolated background of Fig. S9b on top of Fig. S9a.

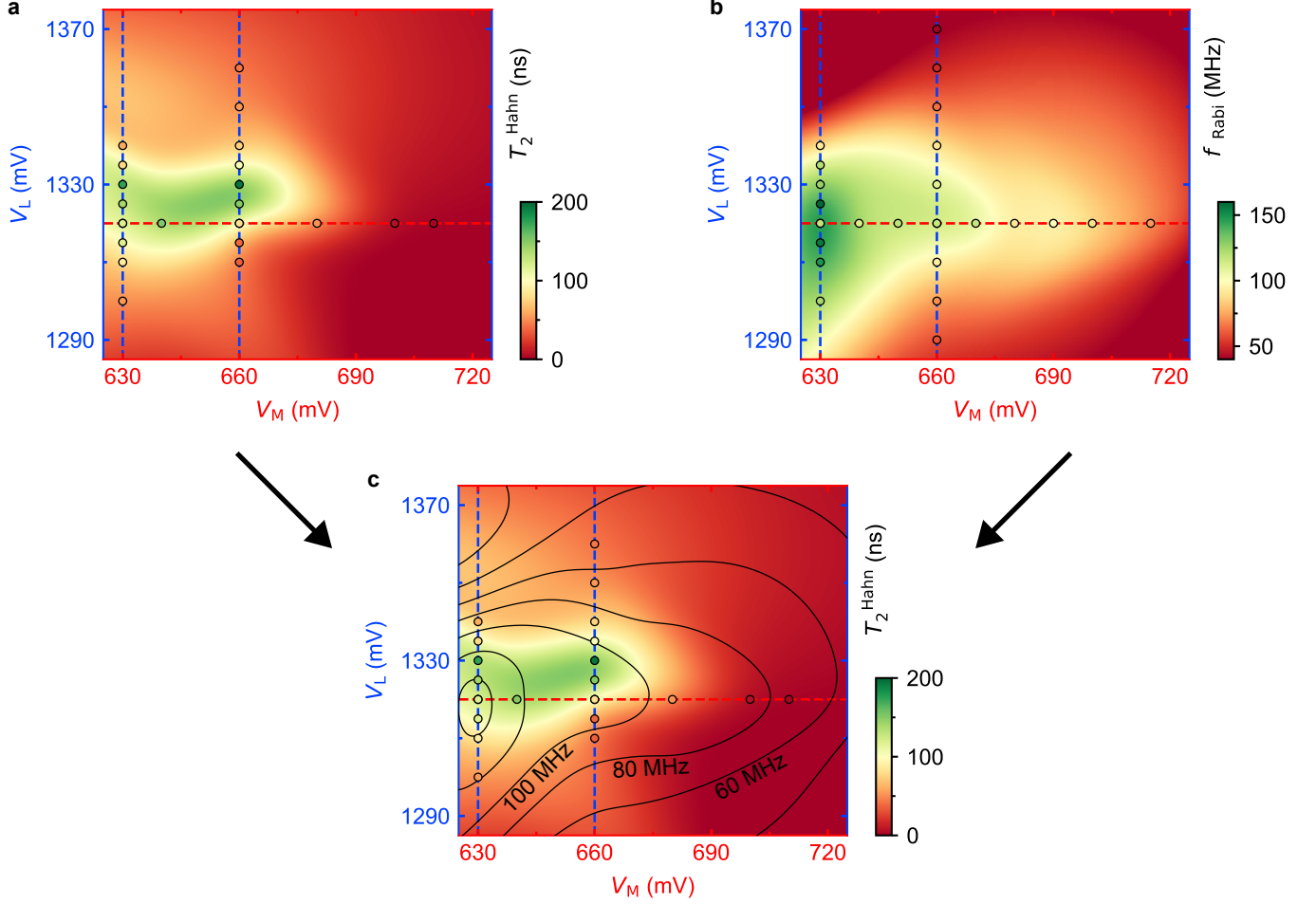


FIG. S9. **2D maps of the FACTOR as a function of  $V_L$  and  $V_M$ .** **a**, 2D voltage space showing  $T_2^{\text{Hahn}}$  as a function of gate voltages  $V_M$  and  $V_L$ . The filled circles represent the measured coherence times  $T_2^{\text{Hahn}}$ . The background is obtained by a Gaussian process interpolation and serves as a guide to the eye. **b**, Analogous to panel a, but for  $f_{\text{Rabi}}$ . **c**, Shows the contours of  $f_{\text{Rabi}}$  from panel b overlaid on the plot of  $T_2^{\text{Hahn}}$  in panel a, to emphasize the overlap of both maxima.

### S9. IMPACT OF CONTROL-AXIS NOISE ON THE COHERENCE $T_2^{\text{Rabi}}$ OF THE DRIVEN QUBIT

When a spin qubit is continuously driven, decoherence from static dephasing is mitigated due to the reduced time spent idling in the equatorial plane. Consequently, noise on the control line becomes more significant.

In the rotating frame of the driven qubit a new basis can be defined known as the dressed basis [24, 25]. In this context, the electromagnetic driving field coherently interacts with the 2-level system of the hole spin, such that the eigenstates of the driven system are no longer the  $|0\rangle$  and  $|1\rangle$  states, but instead the symmetric and antisymmetric superpositions of the spin states entangled with the photons of the driving field. These states constitute a new quantization axis in the driven or *dressed* basis where the two basis states are separated by the Rabi frequency. This change of basis of the main quantization axis shifts the noise spectral function weight towards the Larmor frequency [13].

The decoherence sweet spot is associated with quasi-static dephasing in the equatorial plane and the direction of the externally applied DC-electric field for tuning the *FACTOR* is defined in relation to the main quantization axis in the laboratory frame, commonly set by the external magnetic field. Because the main quantization axis is rotated by  $\pi/2$  relative to the original quantization axis, it is conceivable that the decoherence sweet spot has no significant effect in the rotating frame of the driven spin.

For completeness, we have plotted in Fig. S10 below the  $T_2^{\text{Rabi}}$  data versus the control voltage  $V_L$  in the range over which we show the  $T_2^{\text{Hahn}}$  data points and observe no significant dependence over that range, *i.e.* there seems to be no observable extremum in  $T_2^{\text{Rabi}}$ . Provided an almost constant  $T_2^{\text{Rabi}} \approx 45$  ns, if we additionally take into account the Rabi frequencies from Fig. 1 of the Main text, the voltage dependence of the gate quality factor defined as  ${}^gQ = f_{\text{Rabi}} \cdot T_2^{\text{Rabi}}$ , would be solely dependent on the voltage dependence of  $f_{\text{Rabi}}$  and hence the SOI. This would yield gate quality factors ranging from  $\sim 2$  ( $f_{\text{Rabi}} \approx 40$  MHz) to  $\sim 5$  ( $f_{\text{Rabi}} \approx 120$  MHz), and would still yield an extremum of  ${}^gQ$  peaking at the same gate voltage as  $f_{\text{Rabi}}$ .

The experimental parameters and gate voltages  $V_M$  and  $V_R$  were set to the same values as for the data presented in Fig. 1a of the Main Section and are reported in the Methods Section.

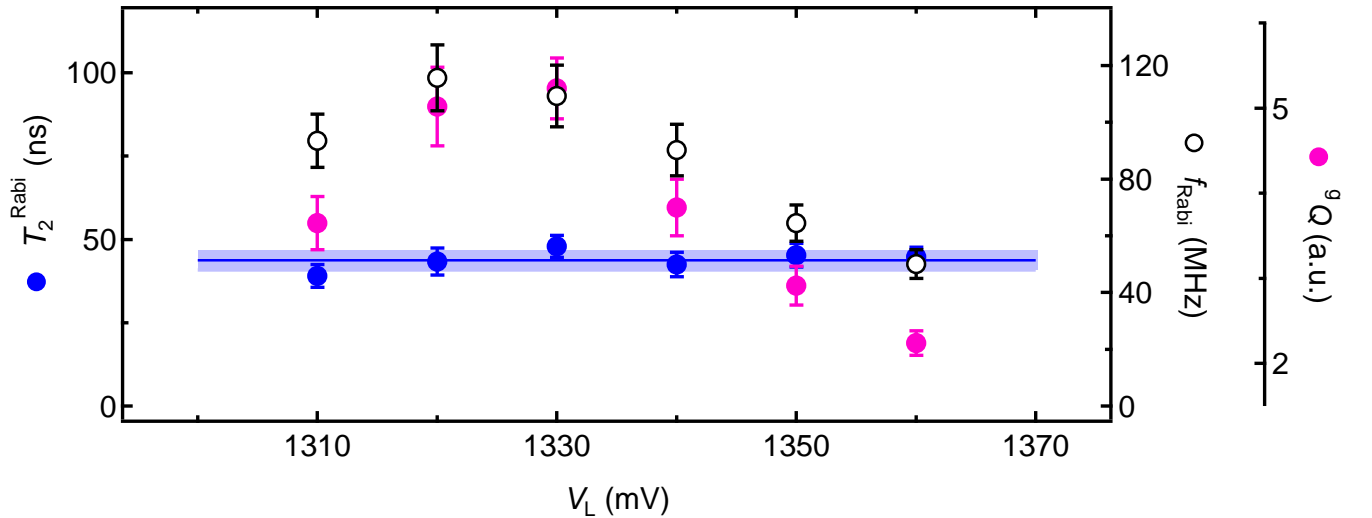


FIG. S10. **Coherence time  $T_2^{\text{Rabi}}$  of the driven spin.** The blue data points show the  $1/e$  decay time of the Rabi oscillations (left axis) as a function of the gate control parameter  $V_L$  over the same range as shown in Fig. 2 of the main text. The blue line highlights the average value of  $T_2^{\text{Rabi}} \approx 45$  ns and standard deviation  $\sigma \approx \pm 3$  ns. For reference, the Rabi frequency  $f_{\text{Rabi}}$  (white) as well as the gate quality factor  ${}^gQ = f_{\text{Rabi}} \cdot T_2^{\text{Rabi}}$  (pink) are also plotted for the corresponding gate voltages (right axes). Error bars for  $T_2^{\text{Rabi}}$  and  $f_{\text{Rabi}}$  correspond to standard deviations that result from fitting. These errors were propagated to obtain the error bars for  ${}^gQ$ .

- 
- [1] C. Klossel, M. Trif, P. Stano, and D. Loss, *Physical Review B* **88**, 241405 (2013).
- [2] S. Bosco, M. Benito, C. Adelsberger, and D. Loss, *Physical Review B* **104**, 115425 (2021).
- [3] V. N. Golovach, M. Borhani, and D. Loss, *Physical Review B* **74**, 165319 (2006).
- [4] C. Klossel, M. J. Rančić, and D. Loss, *Physical Review B* **97**, 235422 (2018).
- [5] G. Scappucci, C. Klossel, F. A. Zwanenburg, D. Loss, M. Myronov, J.-J. Zhang, S. De Franceschi, G. Katsaros, and M. Veldhorst, *Nature Reviews Materials* **6**, 926 (2020).
- [6] L. A. Terrazos, E. Marcellina, Z. Wang, S. N. Coppersmith, M. Friesen, A. R. Hamilton, X. Hu, B. Koiller, A. L. Saraiva, D. Culcer, and R. B. Capaz, *Physical Review B* **103**, 125201 (2021).
- [7] R. Winkler, "Spin-orbit coupling effects in two-dimensional electron and hole systems," (2003).
- [8] C. Adelsberger, M. Benito, S. Bosco, J. Klinovaja, and D. Loss, *Physical Review B* **105**, 075308 (2022).
- [9] C. Klossel, M. Trif, and D. Loss, *Physical Review B* **84**, 195314 (2011).
- [10] S. Bosco, B. Hetényi, and D. Loss, *PRX Quantum* **2**, 010348 (2021).
- [11] A. Crippa, R. Maurand, L. Bourdet, D. Kotekar-Patil, A. Amisse, X. Jehl, M. Sanquer, R. Laviéville, H. Bohuslavskyi, L. Hutin, S. Barraud, M. Vinet, Y.-M. Niquet, and S. D. Franceschi, *Physical Review Letters* **120**, 137702 (2018).
- [12] S. Bosco, P. Scarlino, J. Klinovaja, and D. Loss, *Physical Review Letters* **129**, 066801 (2022).
- [13] S. Bosco, S. Geyer, L. C. Camenzind, R. S. Eggli, A. Fuhrer, R. J. Warburton, D. M. Zumbühl, J. C. Egues, A. V. Kuhlmann, and D. Loss, *Physical Review Letters* **131**, 197001 (2023).
- [14] M. Trif, V. N. Golovach, and D. Loss, *Physical Review B* **77**, 045434 (2008).
- [15] W. Lu, J. Xiang, B. P. Timko, Y. Wu, and C. M. Lieber, *Proceedings of the National Academy of Sciences* **102**, 10046 (2005).
- [16] J. Yoneda, K. Takeda, T. Otsuka, T. Nakajima, M. R. Delbecq, G. Allison, T. Honda, T. Kodera, S. Oda, Y. Hoshi, N. Usami, K. M. Itoh, and S. Tarucha, *Nature Nanotechnology* **13**, 102 (2017).
- [17] D. Culcer, X. Hu, and S. Das Sarma, *Applied Physics Letters* **95** (2009), 10.1063/1.3194778.
- [18] D. K. Schroder, "Semiconductor material and device characterization," (2005).
- [19] L. Massai, B. Hetényi, M. Mergenthaler, F. J. Schupp, L. Sommer, S. Paredes, S. W. Bedell, P. Harvey-Collard, G. Salis, A. Fuhrer, and N. W. Hendrickx, *Communications Materials* **5** (2024), 10.1038/s43246-024-00563-8.
- [20] N. Sangwan, E. Jutzi, C. Olsen, S. Vogel, A. Nigro, I. Zardo, and A. Hofmann, *arXiv* (2024), 10.48550/ARXIV.2411.03995.
- [21] Y. Hu, F. Kuemmeth, C. M. Lieber, and C. M. Marcus, *Nature Nanotechnology* **7**, 47 (2011).
- [22] V. P. Michal, J. C. Abadillo-Uriel, S. Zihlmann, R. Maurand, Y.-M. Niquet, and M. Filippone, *Physical Review B* **107**, 1041303 (2023).
- [23] N. Piot, B. Brun, V. Schmitt, S. Zihlmann, V. P. Michal, A. Apra, J. C. Abadillo-Uriel, X. Jehl, B. Bertrand, H. Niebojewski, L. Hutin, M. Vinet, M. Urdampilleta, T. Meunier, Y.-M. Niquet, R. Maurand, and S. D. Franceschi, *Nature Nanotechnology* **17**, 1072 (2022).
- [24] A. Laucht, R. Kalra, S. Simmons, J. P. Dehollain, J. T. Muhonen, F. A. Mohiyaddin, S. Freer, F. E. Hudson, K. M. Itoh, D. N. Jamieson, J. C. McCallum, A. S. Dzurak, and A. Morello, *Nature Nanotechnology* **12**, 61 (2016).
- [25] A. Laucht, S. Simmons, R. Kalra, G. Tosi, J. P. Dehollain, J. T. Muhonen, S. Freer, F. E. Hudson, K. M. Itoh, D. N. Jamieson, J. C. McCallum, A. S. Dzurak, and A. Morello, *Physical Review B* **94**, 161302 (2016).